

## Communication

### Quantum interference in graphene nanoconstrictions

Pascal Gehring, Hatef Sadeghi, Sara Sangtarash, Chit Siong Lau, Junjie Liu, Arzhang Ardavan, Jamie H. Warner, Colin J. Lambert, G. Andrew D. Briggs, and Jan A. Mol

*Nano Lett.*, **Just Accepted Manuscript** • DOI: 10.1021/acs.nanolett.6b01104 • Publication Date (Web): 13 Jun 2016

Downloaded from <http://pubs.acs.org> on June 14, 2016

#### Just Accepted

“Just Accepted” manuscripts have been peer-reviewed and accepted for publication. They are posted online prior to technical editing, formatting for publication and author proofing. The American Chemical Society provides “Just Accepted” as a free service to the research community to expedite the dissemination of scientific material as soon as possible after acceptance. “Just Accepted” manuscripts appear in full in PDF format accompanied by an HTML abstract. “Just Accepted” manuscripts have been fully peer reviewed, but should not be considered the official version of record. They are accessible to all readers and citable by the Digital Object Identifier (DOI®). “Just Accepted” is an optional service offered to authors. Therefore, the “Just Accepted” Web site may not include all articles that will be published in the journal. After a manuscript is technically edited and formatted, it will be removed from the “Just Accepted” Web site and published as an ASAP article. Note that technical editing may introduce minor changes to the manuscript text and/or graphics which could affect content, and all legal disclaimers and ethical guidelines that apply to the journal pertain. ACS cannot be held responsible for errors or consequences arising from the use of information contained in these “Just Accepted” manuscripts.



ACS Publications

Nano Letters is published by the American Chemical Society, 1155 Sixteenth Street N.W., Washington, DC 20036

Published by American Chemical Society. Copyright © American Chemical Society. However, no copyright claim is made to original U.S. Government works, or works produced by employees of any Commonwealth realm Crown government in the course of their duties.

# Quantum interference in graphene nanoconstrictions

Pascal Gehring<sup>1,\*</sup>, Hatef Sadeghi<sup>2</sup>, Sara Sangtarash<sup>2</sup>, Chit Siong Lau<sup>1</sup>, Junjie Liu<sup>1</sup>, Arzhang Ardavan<sup>3</sup>,  
Jamie H. Warner<sup>1</sup>, Colin J. Lambert<sup>2</sup>, G. Andrew. D. Briggs<sup>1</sup>, Jan A. Mol<sup>1</sup>

<sup>1</sup>*Department of Materials, University of Oxford, 16 Parks Road, Oxford OX1 3PH, United Kingdom*

<sup>2</sup>*Quantum Technology Centre, Physics Department, Lancaster University, Lancaster LA1 4YB, United Kingdom*

<sup>3</sup>*Clarendon Laboratory, Department of Physics, University of Oxford, Parks Road, Oxford OX1 3PU, United Kingdom*

\*[pascal.gehring@materials.ox.ac.uk](mailto:pascal.gehring@materials.ox.ac.uk)

## Abstract

**We report quantum interference effects in the electrical conductance of chemical vapour deposited graphene nanoconstrictions fabricated using feedback controlled electroburning. The observed multi-mode Fabry-Pérot interferences can be attributed to reflections at potential steps inside the channel. Sharp anti-resonance features with a Fano line shape are observed. Theoretical modelling reveals that these Fano resonances are due to localised states inside the constriction, which couple to the delocalised states that also give rise to the Fabry-Pérot interference patterns. This study provides new insight into the interplay between two fundamental forms of quantum interference in graphene nanoconstrictions.**

**KEYWORDS:** graphene, quantum interference, Fano resonance, break junction, Fabry-Pérot

A key feature of electron transport through single molecules and phase-coherent nanostructures is the appearance of transport resonances associated with quantum interference.<sup>1</sup> Examples include Breit-Wigner resonances, multi-path Fabry-Pérot resonances and Fano resonances. Fano resonances can be observed when a localised state interacts with a continuum of extended states and can lead to very steep gradients in the transmission. Unlike Breit-Wigner resonances, they are not life-time broadened

1  
2  
3 by coupling to the electrodes. The steep slope of Fano resonances makes them attractive for low-  
4 power switching and for creating structures with high thermoelectric performance.<sup>2</sup> In what follows,  
5 we report the first observation of Fano resonances in electroburnt graphene nanoconstrictions. In  
6 addition to these Fano features, the conductance maps exhibit interference patterns which we attribute  
7 to multi-mode Fabry-Pérot (FP) interferences. Theoretical modelling reveals that the Fano resonances  
8 arise from interaction between the delocalised state giving rise to the Fabry-Pérot pattern and a  
9 localised state inside the constriction.  
10

11  
12  
13 Carbon-based nanostructures, such as metallic or semiconducting single carbon chains<sup>3, 4</sup>, graphene  
14 nanoribbons and graphene nanoconstrictions are interesting platforms for the study of spintronics<sup>5</sup> and  
15 might enable novel technological applications<sup>6</sup>. Graphene nanoconstrictions and nanogaps also  
16 provide a robust platform for studying the electric<sup>7</sup>, thermoelectric<sup>8</sup> and magnetic<sup>9</sup> properties of single  
17 molecules. When they are sufficiently narrow, graphene nanoribbons can be used to build field-effect  
18 transistors with an on/off ratio that can exceed 1000.<sup>10</sup> In very narrow constrictions, with a width  
19 smaller than the electronic wavelength of electrons, quantum interference effects in analogy to  
20 subwavelength optics are predicted<sup>11, 12</sup>. Graphene nanoconstrictions have been fabricated by means of  
21 electron beam lithography<sup>13</sup>, gold break-junction etching masks<sup>10</sup>, local gating<sup>14</sup> and electroburning of  
22 graphene<sup>15, 16</sup>. Electroburning has also been used to fabricate graphene quantum dots with addition  
23 energies up to 1.6 eV, enabling the observation of Coulomb blockade at room temperature<sup>17</sup>. In this  
24 study we use feedback-controlled electroburning to narrow down lithographically-defined bowtie  
25 shaped graphene constrictions<sup>18</sup> and study their electronic transport behaviour.  
26  
27

28  
29  
30 Our devices are fabricated from single-layer CVD-grown graphene<sup>19</sup> which we transfer onto a  
31 Si/300nm SiO<sub>2</sub> wafer with pre-patterned 10 nm Cr / 70 nm Au contacts. We pattern the graphene into  
32 a bowtie shape (see Figure 1a,b) using standard electron beam lithography and O<sub>2</sub> plasma etching.  
33 The channel length  $L$  of the devices and the width  $W$  of the narrowest part of the constriction are 4  $\mu\text{m}$   
34 and 200 nm, respectively (see Figure 1a). Our devices are p-doped with a Dirac point  $V_{\text{Dirac}}$  around 60  
35 V (see Figure 1c). The single-layer nature of the graphene constriction is confirmed by the intensity  
36 ratio  $I(2D) / I(G) \gg 1$  of the Raman G and 2D peaks (see Figure 1d) and the fact that the 2D peak  
37  
38  
39  
40  
41  
42  
43  
44  
45  
46  
47  
48  
49  
50  
51  
52  
53  
54  
55  
56  
57  
58  
59  
60

1  
2  
3 consists of a single Lorentzian.<sup>20, 21</sup> In addition, we observe a D and D' peak which we attribute to the  
4 defective graphene edges formed during the plasma etching.<sup>21</sup> These defect peaks are not present in  
5 bulk single-layer graphene samples.<sup>19</sup> To narrow down the constriction we use a feedback-controlled  
6 electroburning technique in air, similar to the one described in Ref<sup>18</sup>. We ramp-up a voltage applied  
7 between the source and drain contact while monitoring the current with a 5 kHz sampling rate (see  
8 Figure 1b). As soon as a drop in the current is detected, the voltage is quickly ramped back to zero.  
9 This cycle is repeated until the low bias source-drain resistance of the device, which is measured after  
10 each burning cycle, exceeds a threshold resistance of 500 M $\Omega$ . The feedback conditions are adjusted  
11 for each burning cycle depending on the threshold voltage  $V_{th}$  at which the drop in the previous cycle  
12 occurred. The current-voltage ( $I - V_b$ ) traces of a typical electroburning process are shown in Figure  
13 1e, where the  $I - V_b$  traces before electroburning and after the threshold resistance is reached are  
14 coloured blue and red, respectively.  
15  
16  
17  
18  
19  
20  
21  
22  
23  
24  
25  
26

27  
28 During electroburning, the constriction is narrowed down and as a result the resistance of the device  
29 increases. At the final stage, the (only several atoms wide) constriction can break completely and a  
30 nanometre sized gap is formed.<sup>12</sup> However, for many devices the threshold resistance is reached  
31 before a gap is fully formed. In these cases, narrow graphene constrictions or small graphene islands  
32 are left between the mesoscopic graphene leads. Graphene quantum dots formed in this manner have  
33 been widely studied<sup>15-17, 22</sup> as a possible platform for room temperature single-electron transistors. In  
34 the following we discuss the details of the transport characteristics of empty graphene nanogaps,  
35 quantum dots and nanoconstrictions recorded at  $T = 4$  K in vacuum ( $\sim 10^{-6}$  mbar).  
36  
37  
38  
39  
40  
41  
42  
43  
44

45 The transport regime which we attribute to an empty gap is characterised by low currents and  $I - V_b$   
46 characteristics that can be fitted using the standard Simmons model<sup>23</sup> for tunnelling through a single  
47 trapezoidal barrier between source and drain (see Figure 2a). In addition, the  $I - V_b$  characteristics  
48 show no or a relatively small back gate dependence (see Figure 2b). We find gap sizes of 0.5 – 2.5 nm  
49 for these junctions, making them a promising platform for single molecule electronics.<sup>7, 24, 25</sup>  
50  
51  
52  
53  
54  
55

56 Devices in the weakly coupled quantum dot regime show suppressed current at low bias (see Figure  
57 2c) and characteristic Coulomb diamonds as a function of bias and gate voltage (see Figure 2d). These  
58  
59  
60

1  
2  
3 transport features are indicative of sequential electron tunnelling via a weakly coupled quantum dot  
4 between source and drain.<sup>26</sup> From the size of the Coulomb diamonds we can extract addition energies  
5 for these quantum dots ranging from 20 to 800 meV, comparable to those found by other groups in  
6 similar systems.<sup>13, 15-17</sup> The formation of graphene quantum dots during electroburning process is the  
7 result of electron/hole localisation due to charge puddles and/or edge disorder as the graphene channel  
8 gets narrower.<sup>27</sup> Theoretical calculations have also shown that localised states can form along the  
9 edges of wedge-shaped nanoconstrictions.<sup>28</sup> Furthermore, it is possible that small graphene islands on  
10 the order of several nm form, which are only weakly coupled to the graphene leads.<sup>17</sup>

11  
12  
13  
14  
15  
16  
17  
18  
19  
20 The conductance maps of strongly-coupled devices are dominated by “chess board”-like interference  
21 patterns as shown in Figure 2f. In some samples we could observe a transition from this chess board  
22 pattern to a Coulomb diamond regime at high positive gate voltages of  $\gtrsim 40$ V. This observation is  
23 similar to results found in recent studies on short graphene junctions<sup>29, 30</sup> and narrow graphene  
24 constrictions<sup>31</sup>. In the latter, the chess board pattern was attributed to interference effects of extended  
25 states in the source or drain graphene lead connecting the constriction.<sup>31</sup> In general, interference  
26 effects occur on a length scale on the order of the phase coherence length, but can have different  
27 origins. If the transport in the graphene sample is diffusive, i.e. when charge carriers are  
28 predominantly scattered at random impurities like edge disorder, point defects or charge puddles,<sup>27</sup> the  
29 origin of the interference pattern is most likely due to quantum interferences of different random  
30 scattering paths (universal conductance fluctuations, UCFs). If the channel length is on the order of or  
31 shorter than the mean free path of the carriers (quasi-ballistic transport regime), reflections in the  
32 channel result in quasi-periodic multi-mode or collective and periodic single-mode Fabry-Pérot  
33 interferences. Carriers can get reflected at the metal contacts<sup>30</sup> or at potential barriers formed by  
34 intentional local doping.<sup>32</sup> Whether single- or multi-mode interference is observed strongly depends  
35 on the detailed device geometry.<sup>33</sup>

36  
37  
38  
39  
40  
41  
42  
43  
44  
45  
46  
47  
48  
49  
50  
51  
52  
53 Fabry-Pérot interference effects have previously been observed in 1D nanowires<sup>34</sup>, carbon nanotubes<sup>35</sup>  
54 and 2D graphene<sup>30</sup>, while UCFs have been observed in mesoscopic single-<sup>36</sup>, bi- and tri-layer<sup>37</sup> and  
55 epitaxial graphene samples<sup>38</sup>. To distinguish between these different types of quantum interference,  
56  
57  
58  
59  
60

1  
2  
3 the chess board conductance patterns need to be carefully analysed for hidden periodicities.<sup>30</sup> From  
4 the characteristic energy spacing between single features in the conductance maps and Fast Fourier  
5 Transforms (FFTs) of the data shown in Figure 2f (see Figure S6a and b in the Supplementary  
6 Information) we can extract a typical energy spacing of 4 – 5 meV. Using a particle-in-a-box  
7 approximation<sup>30</sup> we estimate the relevant length scale  $L = h v_F / (2E)$  to be between 400 nm for the  
8 theoretical local density approximation limit of the Fermi velocity of  $v_F = 0.8 \times 10^6$  m/s and 1.1  $\mu\text{m}$  for  
9 a Fermi velocity of  $v_F = 2.4 \times 10^6$  m/s measured for CVD graphene on a quartz substrate.<sup>39</sup> This length  
10 scale corresponds to half the minimal distance over which the electrons remain phase coherent,  
11 therefore we can infer a lower bound for the phase coherence length  $L_\phi > 800$  nm in our samples.<sup>29</sup>  
12 This value is similar to the value found for exfoliated graphene on  $\text{SiO}_2$ ,<sup>40</sup> epitaxial graphene<sup>41</sup> and  
13 CVD graphene<sup>42</sup>. For short and wide devices small incident angles dominate (longitudinal modes) and  
14 resonances appear at  $k_F L = n\pi$ .<sup>32</sup> However, since our devices are not in the limit  $W/L \gg 1$ , both  
15 longitudinal and transversal modes need to be considered. To model conductance maps for different  
16 aspect ratios we have performed nearest-neighbour tight-binding calculations<sup>33</sup> (see section S5  
17 Supplementary Information). Our calculations confirm that for  $W \gg L$  a periodic interference pattern  
18 with high contrast can be observed. This is due to the fact that the energy of transversal modes  $E_W =$   
19  $h v_F / (2W)$  gets negligibly small. The same holds for the 1D limit  $W \rightarrow 0$ , where  $E_W$  goes to infinity. In  
20 both cases the transport is dominated by longitudinal modes only. In the intermediate multi-mode  
21 regime, periodic longitudinal modes can still be observed in the FFT but with much smaller contrast.  
22 Since the aspect ratio  $W/L$  of our devices is close to unity we expect that the interference pattern  
23 shown in Figure 2b will only be quasi-periodic because of multi-mode interferences. Moreover, the  
24 fact that the width  $W$  of the samples is not constant will cause the transversal modes to become  
25 chaotic.<sup>11</sup>

26  
27  
28  
29  
30  
31  
32  
33  
34  
35  
36  
37  
38  
39  
40  
41  
42  
43  
44  
45  
46  
47  
48  
49  
50 Because the measured chess board pattern is only quasi-periodic, we cannot exclude UCFs as an  
51 origin of the observed pattern. UCFs are normally most pronounced at low doping concentrations  
52 when the electrochemical potential of graphene is close to the Dirac point.<sup>30</sup> This is unlikely to be the  
53 case in our  $p$ -doped graphene junctions. In addition, the periodicity which we can correlate with the  
54  
55  
56  
57  
58  
59  
60

1  
2  
3 geometry of the device is very similar for all devices investigated in this study, which makes multi-  
4 mode Fabry-Pérot interferences a more likely mechanism to explain our data.  
5  
6

7  
8 Next, we will investigate the microscopic origin of the FP reflections. Based on our assumption for  
9 the Fermi velocity (see above) we estimate that carriers are coherently reflected on a length scale of  $\sim$   
10 1  $\mu\text{m}$ . The visibility/intensity of FP interferences is determined by the reflectance of the potential  
11 steps. Unipolar cavities have a small finesse and result in a small visibility  $(G_{\text{max}} - G_{\text{min}}) / (G_{\text{max}} +$   
12  $G_{\text{min}})$  since the conservation of pseudospin suppresses backscattering in graphene.<sup>32</sup> A smooth bipolar  
13 potential step like a  $pn$  junction formed near a metal-graphene contact has a much higher finesse and  
14 leads to pronounced resonance pattern.<sup>32</sup> However, since the length scale of less than 1  $\mu\text{m}$  found  
15 above is much smaller than the channel length of 4  $\mu\text{m}$  of our devices there need to be additional  
16 potential steps inside the graphene channel apart from the metal contacts. From scanning electron  
17 microscopy and micro Raman spectroscopy (see Sections S1 and S4 in the Supplementary  
18 Information) we can infer that the local hole concentration within a region of several hundreds of nm  
19 around the graphene constriction is increased during electroburning. The increase of hole doping of  
20 graphene on  $\text{SiO}_2$  annealed in air was intensively studied and attributed to doping by  $\text{O}_2$  and moisture  
21 and a change in the degree of coupling between graphene and  $\text{SiO}_2$ .<sup>43</sup> This increased p doping can  
22 result in the formation of a  $pp^+p$  junction in the central region of the devices (see Figure S6c and d in  
23 the Supplementary Information). Possible resonance conditions are reflections between the gold  
24 contact/the  $pn$  junction close to the gold contact and the  $pp^+p$  junction or reflections within the  $pp^+p$   
25 junction which all have a characteristic length scale of several hundreds of nm. This length scale is on  
26 the order of the-mean-free path of charge carriers in our devices (see Supplementary Information),  
27 which further corroborates our interpretation that the chess board pattern arises from FP interferences  
28 rather than scattering at random impurities inside the channel. The visibility of the FP interferences  
29  $(G_{\text{max}} - G_{\text{min}}) / (G_{\text{max}} + G_{\text{min}}) > 10\%$  is high in our devices, which indicates that the unipolar  $p^+p$   
30 interfaces need to have a sharp potential drop with  $k_{\text{F}}d \ll 1$ , where  $d$  is the length over which the  
31 carrier density changes.<sup>44</sup> We estimate this length scale by calculating the Fermi vector using  $n = k_{\text{F}}^2/\pi$   
32  
33  
34  
35  
36  
37  
38  
39  
40  
41  
42  
43  
44  
45  
46  
47  
48  
49  
50  
51  
52  
53  
54  
55  
56  
57  
58  
59  
60

1  
2  
3 and the charge carrier concentration  $n = C_g^2(V_g - V_{\text{Dirac}})^2/e^2$ ,<sup>30</sup> where  $C_g$  is the capacitance of the  
4 back gate and  $e$  is the elementary charge. For  $V_{\text{Dirac}} = 60$  V (see Figure 1c),  $d$  is on the order of 3 nm.  
5  
6

7  
8 We only see interference patterns in nearly fully-burned devices and not directly after the first  
9 electroburning steps. We attribute this to the decreasing conductance of the graphene constriction  
10 during electroburning, which decreases the denominator in  $(G_{\text{max}} - G_{\text{min}}) / (G_{\text{max}} + G_{\text{min}})$  and thus  
11 increases the visibility of the interferences. Another possible explanation for the onset of interference  
12 pattern after electroburning is the recrystallisation of the constriction,<sup>45</sup> which may lead to a higher  
13 mean free path that is required for reflections on the  $\mu\text{m}$  scale. The interplay between reduced width  
14 and reduced carrier density may also increase the factor  $\lambda/W$ , where  $\lambda = hv_F/E$  is the wavelength of  
15 the electrons. If this ratio becomes  $\gtrsim 3 - 5$  the Fabry-Pérot interferences have a high contrast.<sup>11</sup>  
16  
17  
18  
19  
20  
21  
22  
23

24  
25 We now turn to the sharp anti-resonances in the interference regime as shown in Figure 3a and b  
26 (around  $V_g = -18$  V) in some samples (see Supplementary Information for data of other samples). The  
27 slope of this anti-resonance feature is different from the slopes of the multi-mode FP interference  
28 patterns. Repeated thermal cycling from 4 K to room temperature did not change the slope and  
29 position of the feature observed at 4K (see Figure S8). The feature consists of an anti-  
30 resonance/resonance double-peak as shown in Figure 3c. This asymmetric curve has a distinct Fano  
31 line shape,<sup>46</sup> which is the result of coherent interaction between a localised resonant state with a  
32 delocalised background state.<sup>1</sup> Fano resonances have previously been observed in double donor  
33 systems in nanoscale silicon transistors<sup>47</sup> and in bundles of single walled CNTs<sup>48</sup>. Fano resonances are  
34 also predicted for single molecule systems, where a backbone state is coupled to the leads and a  
35 pendant side-group is only coupled to the backbone but not to the leads.<sup>1</sup> In a graphene constriction  
36 connected to mesoscopic graphene leads there are delocalised states that give rise to the previously  
37 discussed FP pattern, and bound states e.g. localised along the edges due to edge roughness, that give  
38 rise to Coulomb blockade at high positive gate voltages close to the Dirac point (see Figure 2f).<sup>31</sup> We  
39 attribute the observed Fano resonances to the coherent interaction between these states.  
40  
41  
42  
43  
44  
45  
46  
47  
48  
49  
50  
51  
52  
53  
54  
55  
56  
57  
58  
59  
60



To estimate the coherent coupling strength between the localised and delocalised states in the graphene nanoconstriction, we fit the low bias current – gate voltage ( $I - V_g$ ) traces to the Fano formula:<sup>48, 49</sup>

$$G(\varepsilon) = G_{\text{non}} + G_{\text{res}} \frac{(\varepsilon + q)^2}{\varepsilon^2 + 1}, \quad (1)$$

where  $G_{\text{res}}$  is the coherent contribution to the conductance,  $q$  is the complex Fano factor,<sup>50</sup>  $\varepsilon = 2(E - \varepsilon_s)/\Gamma_{\text{Fano}}$ ,  $\varepsilon_s$  and  $\Gamma_{\text{Fano}}$  are the energy and coupling strength of the resonant localised state and  $G_{\text{non}}$  is the conductance of the non-resonant channel. We model the non-resonant background as the sum of a constant offset  $G_{\text{off}}$  and a Breit-Wigner peak  $A \frac{\Gamma^2}{\Gamma^2 + (E - \varepsilon_b)^2}$ . This non-resonant background accounts for the conductance peak close to the observed anti-resonance feature. Fits to our data at different bias voltages using Equation (1) are shown as solid lines in Figure 3c. We find for a low bias of  $V_b = 0.1$  mV:  $\varepsilon_s = -18.3$  meV,  $\text{Re}(q) = 0.3$ ,  $\text{Im}(q) = 1.1$ ,  $|q| = 1.1$ ,  $\Gamma_{\text{Fano}} = 0.4$  meV, and a Breit-Wigner peak at  $\varepsilon_b = -20.5$  meV with a coupling strength of  $\Gamma = 1.1$  meV using a lever arm  $dE/dV_g$  of 1 meV/V extracted from the slope of the Fabry-Pérot interference pattern as depicted by the dotted black line in Figure 3a. The Fano factor  $q$  is a combined measure for the energetic detuning and the ratio of the transmission amplitudes of the resonant and the non-resonant channel.<sup>49</sup> For  $q \rightarrow \infty$ , the transport is dominated by the resonant channel and the line shape becomes that of a Breit-Wigner peak. For  $q \rightarrow 0$  non-resonant transport dominates resulting in a symmetric dip in the conductance.<sup>49</sup> The value of  $|q| = 1.1$  found in our experiments results in an asymmetric feature with characteristic Fano line-shape.<sup>48</sup> The width of  $\Gamma_{\text{Fano}} = 0.4$  meV of the resonant state is similar to the values of 0.25 – 0.5 meV found for carbon nanotube bundles.<sup>48</sup> The Fano factor  $q$  decreases with increasing positive bias voltage (see inset in Figure 3c) which we attribute to a detuning of the energies of the localised state and the extended states. For large negative bias voltages the detuning changes the Fano factor from 1 to a high value, and the transport is dominated by a resonant channel resulting in a Breit-Wigner peak. The slope of the Fano feature, as seen in Figure 3a, results from the electrostatic coupling of the localised ‘pendant’ state to the gate and lead electrodes. Figure 4a, shows a tight-binding model of a pendant state interacting with an extended ‘backbone’ state. A chain of 5 sites acts as the backbone,

1  
2  
3 while a single site coupled to the second site of the backbone serves as pendant group. Figure 4b  
4 shows the calculated transmission coefficient  $T(E)$  as a function of energy  $E$ . A Fano-resonance  
5 appears at an energy of about 0.5 eV, which is associated with the site energy of the bound state. The  
6 various transmission maxima are Fabry-Pérot resonances of the backbone channel. To calculate the  
7 differential conductance characteristic  $dI/dV_b(V_b, V_g)$  of the device for different gate voltages  $V_g$ , bias  
8 and gate voltage dependent transmission coefficients  $T(E, V_b, V_g)$  were calculated for two different  
9 potential profiles, where i) the bias drops over the left and right contacts (Figure 4c); or ii) the bias  
10 drops along the device channel (Figure 4d). In the case where the bias voltage drops across the  
11 contacts (see Figure 4c), the on-site energies of the pendant group and the backbone are not  
12 influenced by the applied bias voltage. As a consequence the two anti-resonance Fano lines have the  
13 same slope as the Fabry-Pérot interference lines (see Figure 4e). In contrast, when the potential drops  
14 over the channel (see Figure 4d), the slopes of the anti-resonance lines and the backbone resonances  
15 become different (see Figure 4f). As a result of the asymmetry of the junction, one of the Fano lines  
16 almost vanishes (see section S7 in the Supplementary Information for details). Comparing the  
17 calculations in Figure 4e and f with the experimental data in Figure 3a, we can conclude that, firstly,  
18 the investigated junctions are asymmetric and, secondly, that a considerable portion of the applied  
19 voltage has to drop across the junction. In a more realistic model, where two hexagonal lattices are  
20 connected to various scattering regions with and without pendant groups (see Figure 5), Fano  
21 resonances can be only observed in junctions with pendant groups (see section S6 and S8 for more  
22 details). Molecular-dynamics simulations and density functional theory calculations of different  
23 atomic configurations during nanogap formation<sup>12</sup> further show that dangling carbon atoms and edge  
24 disorder can lead to Fano resonance in the transmission spectra of partially burned graphene nanogaps  
25 (see section S8 in the Supplementary Information).

26  
27  
28  
29  
30  
31  
32  
33  
34  
35  
36  
37  
38  
39  
40  
41  
42  
43  
44  
45  
46  
47  
48  
49  
50  
51 In summary we investigated graphene nanoconstrictions fabricated by narrowing down bowtie shaped  
52 graphene ribbons using a feedback controlled electroburning technique. In the case of weakly-coupled  
53 constrictions, the transport is dominated by Coulomb blockade with addition energies up to 800 meV.  
54  
55  
56  
57 In the strongly coupled regime, we observe quasi-periodic chess board like pattern in the conductance  
58  
59  
60

1  
2  
3 maps which we attribute to multi-mode Fabry-Pérot interferences of delocalised states whose length  
4  
5 scale agrees with two possible resonance conditions: reflections inside the current-annealed low-  
6  
7 doped part of the device or reflections between the electrical contacts and the low-doped part. In some  
8  
9 of the devices, we observe sharp anti-resonances features with a Fano line shape inside the  
10  
11 interference regime in agreement with our tight binding modelling. We attribute these features to  
12  
13 interferences between the extended states and localised states inside the constriction. Such sharp anti-  
14  
15 resonances have the potential to underpin the development of low-power switches, because the  
16  
17 transmission of the structure can be tuned by a small gate voltage. Moreover, the Mott formula  
18  
19 predicts that a high  $d\ln G/dV_g$  should also result in a high Seebeck coefficient<sup>51</sup>, making such devices  
20  
21 promising candidates for thermoelectric energy harvesting.  
22  
23  
24  
25  
26

### 27 **Acknowledgements**

28  
29 We thank the Royal Society for a Newton International Fellowship for J. A. M., the Agency for  
30  
31 Science Technology and Research (A\*STAR) for a studentship for C.S.L. and a University Research  
32  
33 Fellowship for J. H. W. This work is supported by Oxford Martin School, the European Commission  
34  
35 (EC) FP7 ITN “MOLESCO” (project no. 606728) and UK EPSRC (grant nos. EP/K001507/1,  
36  
37 EP/J014753/1, EP/H035818/1 and EP/J015067/1). This project/publication was made possible  
38  
39 through the support of a grant from Templeton World Charity Foundation. The opinions expressed in  
40  
41 this publication are those of the author(s) and do not necessarily reflect the views of Templeton World  
42  
43 Charity Foundation. The authors would like to thank D. Gunlycke for his help and the useful  
44  
45 discussions and Y. Fan and J. Nägele for providing supporting transport data.  
46  
47  
48  
49  
50

### 51 **Supporting Information**

52  
53 Supporting SEM images of the devices, Electrical characterization of graphene used in this study,  
54  
55 Supporting micro Raman data, detailed study of interference pattern, additional Fano data, bias  
56  
57 dependence of the Fano feature, molecular-dynamics simulations.  
58  
59  
60

**Corresponding Author**

\*E-mail: <mailto:pascal.gehring@materials.ox.ac.uk>

**References**

1. Lambert, C. J. *Chem. Soc. Rev.* **2015**, *44*, 875-888.
2. Finch, C. M.; Garcia-Suarez, V. M.; Lambert, C. J. *Phys. Rev. B* **2009**, *79*, 033405.
3. Rong, Y. M.; Warner, J. H. *ACS Nano* **2014**, *8*, 11907-11912.
4. Chuvilin, A.; Meyer, J. C.; Algara-Siller, G.; Kaiser, U. *New J. Phys.* **2009**, *11*, 083019.
5. Son, Y. W.; Cohen, M. L.; Louie, S. G. *Nature* **2006**, *444*, 347-349.
6. Pezoldt, J.; Hummel, C.; Hanisch, A.; Hotovy, I.; Kadlecikova, M.; Schwierz, F. *Phys. Status Solidi C* **2010**, *7*, 390-393.
7. Mol, J. A.; Lau, C. S.; Lewis, W. J. M.; Sadeghi, H.; Roche, C.; Cnossen, A.; Warner, J. H.; Lambert, C. J.; Anderson, H. L.; Briggs, G. A. D. *Nanoscale* **2015**, *7*, 13181-13185.
8. Sadeghi, H.; Sangtarash, S.; Lambert, C. J. *Beilstein J. Nanotechnol.* **2015**, *6*, 1413-1420.
9. Candini, A.; Klyatskaya, S.; Ruben, M.; Wernsdorfer, W.; Affronte, M. *Nano Lett.* **2011**, *11*, 2634-2639.
10. Lu, Y.; Goldsmith, B.; Strachan, D. R.; Lim, J. H.; Luo, Z. T.; Johnson, A. T. C. *Small* **2010**, *6*, 2748-2754.
11. Darancet, P.; Olevano, V.; Mayou, D. *Phys. Rev. Lett.* **2009**, *102*, 136803.
12. Sadeghi, H.; Mol, J. A.; Lau, C. S.; Briggs, G. A. D.; Warner, J.; Lambert, C. J. *Proc. Natl. Acad. Sci. U. S. A.* **2015**, *112*, 2658-2663.
13. Ihn, T.; Guttinger, J.; Molitor, F.; Schnez, S.; Schurtenberger, E.; Jacobsen, A.; Hellmuller, S.; Frey, T.; Droscher, S.; Stampfer, C.; Ensslin, K. *Mater. Today* **2010**, *13*, 44-50.
14. Allen, M. T.; Martin, J.; Yacoby, A. *Nat. Commun.* **2012**, *3*, 934.
15. Moser, J.; Bachtold, A. *Appl. Phys. Lett.* **2009**, *95*, 173506.

- 1  
2  
3 16. Ki, D. K.; Morpurgo, A. F. *Phys. Rev. Lett.* **2012**, *108*, 266601.  
4  
5 17. Barreiro, A.; van der Zant, H. S. J.; Vandersypen, L. M. K. *Nano Lett.* **2012**, *12*, 6096-6100.  
6  
7 18. Lau, C. S.; Mol, J. A.; Warner, J. H.; Briggs, G. A. D. *Phys. Chem. Chem. Phys.* **2014**, *16*,  
8  
9 20398-20401.  
10  
11 19. Wu, Y. M. A.; Fan, Y.; Speller, S.; Creeth, G. L.; Sadowski, J. T.; He, K.; Robertson, A. W.;  
12  
13 Allen, C. S.; Warner, J. H. *ACS Nano* **2012**, *6*, 5010-5017.  
14  
15 20. Sun, Z. Z.; Yan, Z.; Yao, J.; Beitler, E.; Zhu, Y.; Tour, J. M. *Nature* **2010**, *468*, 549-552.  
16  
17 21. Ferrari, A. C.; Basko, D. M. *Nat. Nanotechnol.* **2013**, *8*, 235-246.  
18  
19 22. Puczkarski, P.; Gehring, P.; Lau, C. S.; Liu, J. J.; Ardavan, A.; Warner, J. H.; Briggs, G. A.  
20  
21 D.; Mol, J. A. *Appl. Phys. Lett.* **2015**, *107*, 133105.  
22  
23 23. Simmons, J. G. *J. Appl. Phys.* **1963**, *34*, 1793-1803.  
24  
25 24. Lau, C. S.; Sadeghi, H.; Rogers, G.; Sangtarash, S.; Dallas, P.; Porfyraakis, K.; Warner, J.;  
26  
27 Lambert, C. J.; Briggs, G. A. D.; Mol, J. A. *Nano Lett.* **2016**, *16*, 170-176.  
28  
29 25. Burzurí, E.; Island, J. O.; Díaz-Torres, R.; Fursina, A.; González-Campo, A.; Roubeau, O.;  
30  
31 Teat, S. J.; Aliaga-Alcalde, N.; Ruiz, E.; van der Zant, H. S. J. *ACS Nano* **2016**, *10*, 2521-2527.  
32  
33 26. Hanson, R.; Kouwenhoven, L. P.; Petta, J. R.; Tarucha, S.; Vandersypen, L. M. K. *Rev. Mod.*  
34  
35 *Phys.* **2007**, *79*, 1217-1265.  
36  
37 27. Bischoff, D.; Varlet, A.; Simonet, P.; Eich, M.; Overweg, H. C.; Ihn, T.; Ensslin, K. *Appl.*  
38  
39 *Phys. Rev.* **2015**, *2*, 031301.  
40  
41 28. Muñoz-Rojas, F.; Jacob, D.; Fernández-Rossier, J.; Palacios, J. J. *Phys. Rev. B* **2006**, *74*,  
42  
43 195417.  
44  
45 29. Miao, F.; Wijeratne, S.; Zhang, Y.; Coskun, U. C.; Bao, W.; Lau, C. N. *Science* **2007**, *317*,  
46  
47 1530-1533.  
48  
49 30. Oksanen, M.; Uppstu, A.; Laitinen, A.; Cox, D. J.; Craciun, M. F.; Russo, S.; Harju, A.;  
50  
51 Hakonen, P. *Phys. Rev. B* **2014**, *89*, 121414.  
52  
53 31. Bischoff, D.; Libisch, F.; Burgdorfer, J.; Ihn, T.; Ensslin, K. *Phys. Rev. B* **2014**, *90*, 115405.  
54  
55 32. Rickhaus, P.; Maurand, R.; Liu, M. H.; Weiss, M.; Richter, K.; Schonenberger, C. *Nat.*  
56  
57 *Commun.* **2013**, *4*, 2342.  
58  
59  
60

- 1  
2  
3 33. Gunlycke, D.; White, C. T. *Appl. Phys. Lett.* **2008**, *93*, 122106.  
4  
5 34. Kretinin, A. V.; Popovitz-Biro, R.; Mahalu, D.; Shtrikman, H. *Nano Lett.* **2010**, *10*, 3439-  
6  
7 3445.  
8  
9 35. Liang, W. J.; Bockrath, M.; Bozovic, D.; Hafner, J. H.; Tinkham, M.; Park, H. *Nature* **2001**,  
10  
11 *411*, 665-669.  
12  
13 36. Morozov, S. V.; Novoselov, K. S.; Katsnelson, M. I.; Schedin, F.; Ponomarenko, L. A.; Jiang,  
14  
15 D.; Geim, A. K. *Phys. Rev. Lett.* **2006**, *97*, 016801.  
16  
17 37. Staley, N. E.; Puls, C. P.; Liu, Y. *Phys. Rev. B* **2008**, *77*, 155429.  
18  
19 38. Berger, C.; Song, Z. M.; Li, X. B.; Wu, X. S.; Brown, N.; Naud, C.; Mayou, D.; Li, T. B.;  
20  
21 Hass, J.; Marchenkov, A. N.; Conrad, E. H.; First, P. N.; de Heer, W. A. *Science* **2006**, *312*, 1191-  
22  
23 1196.  
24  
25 39. Hwang, C.; Siegel, D. A.; Mo, S. K.; Regan, W.; Ismach, A.; Zhang, Y. G.; Zettl, A.;  
26  
27 Lanzara, A. *Sci. Rep.* **2012**, *2*, 590.  
28  
29 40. Lee, G. H.; Jeong, D.; Choi, J. H.; Doh, Y. J.; Lee, H. J. *Phys. Rev. Lett.* **2011**, *107*, 146605.  
30  
31 41. Lara-Avila, S.; Tzalenchuk, A.; Kubatkin, S.; Yakimova, R.; Janssen, T. J. B. M.; Cedergren,  
32  
33 K.; Bergsten, T.; Fal'ko, V. *Phys. Rev. Lett.* **2011**, *107*, 166602.  
34  
35 42. Baker, A. M. R.; Alexander-Webber, J. A.; Altebaeumer, T.; Janssen, T. J. B. M.;  
36  
37 Tzalenchuk, A.; Lara-Avila, S.; Kubatkin, S.; Yakimova, R.; Lin, C. T.; Li, L. J.; Nicholas, R. J. *Phys.*  
38  
39 *Rev. B* **2012**, *86*, 235441.  
40  
41 43. Ryu, S.; Liu, L.; Berciaud, S.; Yu, Y. J.; Liu, H. T.; Kim, P.; Flynn, G. W.; Brus, L. E. *Nano*  
42  
43 *Lett.* **2010**, *10*, 4944-4951.  
44  
45 44. Cheianov, V. V.; Fal'ko, V. I. *Phys. Rev. B* **2006**, *74*, 041403.  
46  
47 45. Qi, Z. J.; Daniels, C.; Hong, S. J.; Park, Y. W.; Meunier, V.; Drndic, M.; Johnson, A. T. C.  
48  
49 *ACS Nano* **2015**, *9*, 3510-3520.  
50  
51 46. Miroshnichenko, A. E.; Flach, S.; Kivshar, Y. S. *Rev. Mod. Phys.* **2010**, *82*, 2257-2298.  
52  
53 47. Verduijn, J.; Tettamanzi, G. C.; Lansbergen, G. P.; Collaert, N.; Biesemans, S.; Rogge, S.  
54  
55 *Appl. Phys. Lett.* **2010**, *96*, 072110.  
56  
57 48. Babić, B.; Schönenberger, C. *Phys. Rev. B* **2004**, *70*, 195408.  
58  
59  
60

- 1  
2  
3 49. Gores, J.; Goldhaber-Gordon, D.; Heemeyer, S.; Kastner, M. A.; Shtrikman, H.; Mahalu, D.;  
4  
5 Meirav, U. *Phys. Rev. B* **2000**, *62*, 2188-2194.  
6  
7 50. Clerk, A. A.; Waintal, X.; Brouwer, P. W. *Phys. Rev. Lett.* **2001**, *86*, 4636-4639.  
8  
9 51. Cutler, M.; Mott, N. F. *Phys. Rev.* **1969**, *181*, 1336-1340.  
10  
11  
12  
13  
14  
15  
16  
17  
18  
19  
20  
21  
22  
23  
24  
25  
26  
27  
28  
29  
30  
31  
32  
33  
34  
35  
36  
37  
38  
39  
40  
41  
42  
43  
44  
45  
46  
47  
48  
49  
50  
51  
52  
53  
54  
55  
56  
57  
58  
59  
60

**Captions**

**Figure 1.** (a) False colour SEM image of a graphene constriction (grey) contacted by gold contacts (yellow). (b) Schematic of a graphene nanoconstriction device. (c) Conductance as a function of back gate voltage recorded at  $V_b = 100$  mV of an as-prepared device. (d) Raman spectrum of the centre region of the graphene bow-tie after electroburning. (e)  $I - V_b$  traces recorded during feedback-controlled electroburning. The first and last traces are shown in blue and red, respectively.

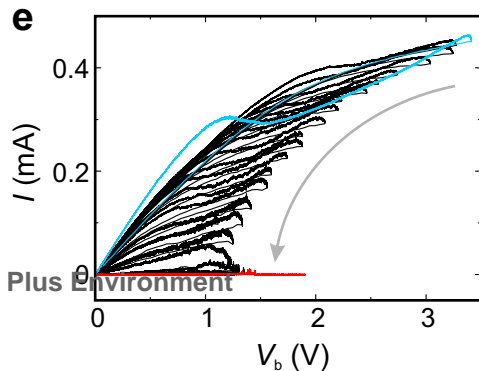
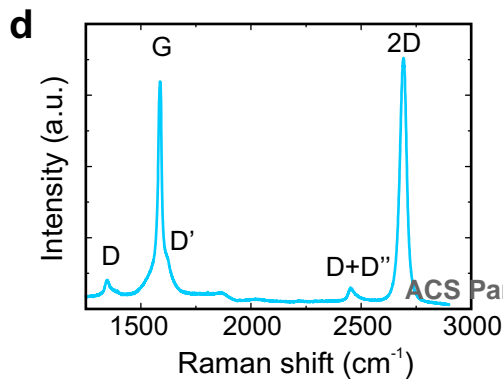
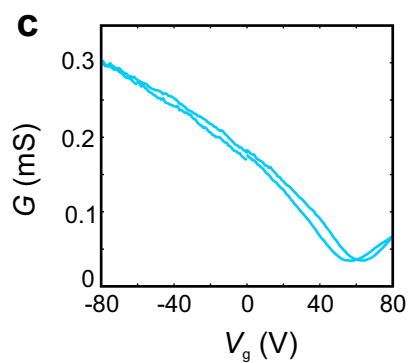
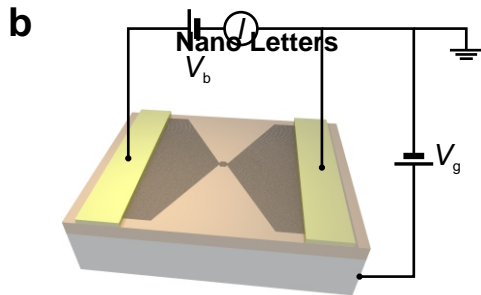
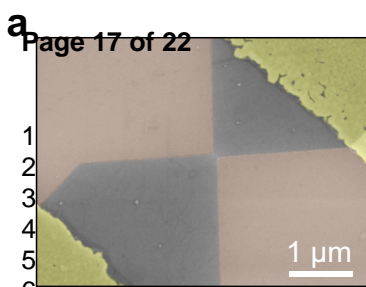
**Figure 2.** Nanostructures with different electronic behaviour formed during electroburning. (a)  $I - V_b$  trace and (b) current map of an empty gap. (c)  $I - V_b$  trace and (d) current map of a weakly coupled constriction showing sequential tunnelling. (e)  $I - V_b$  trace and (f) conductance map of a strongly coupled constriction showing resonance effects. All data was recorded at  $T = 4$  K under vacuum. The insets depict a scheme of the constriction.

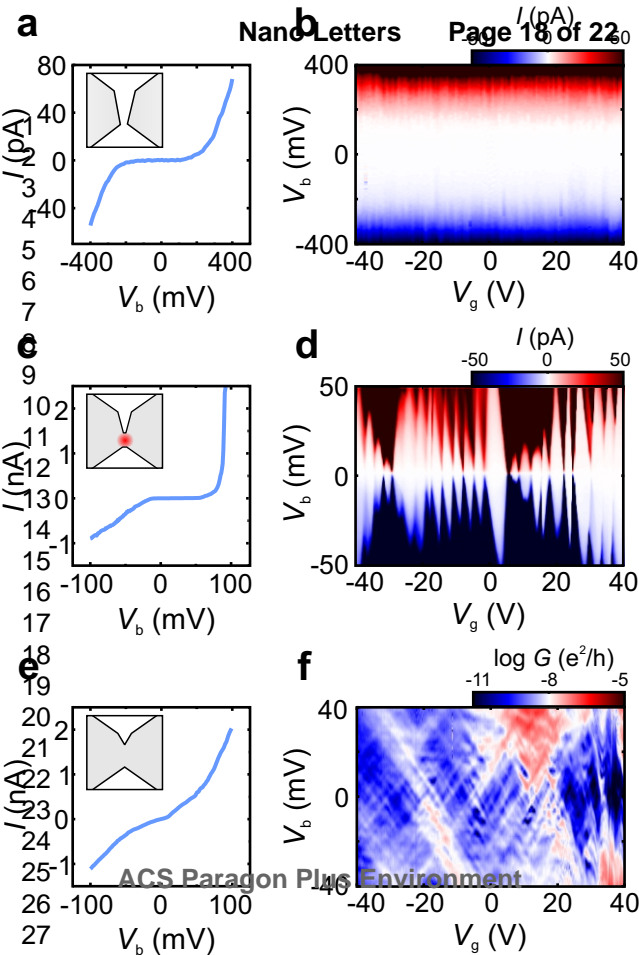
**Figure 3.** (a) Conductance map at  $T = 4$  K of a strongly coupled constriction showing interference effects. A sharp anti-resonance feature around  $V_g = -18$  V can be observed. The dotted line is used to extract the lever arm. (b) Gate traces for different bias voltages  $0.1 \text{ mV} \leq V_b \leq 8 \text{ mV}$  in  $0.2 \text{ mV}$  steps of the data shown in (a). The curves are offset by  $0.2 \times 10^3 e^2/h$  for clarity. (c) Gate traces at different bias voltages (dotted lines) and fits using Equation 1 (solid lines). The inset shows the dependence of the Fano factor  $|q|$  as a function of the applied bias voltage.

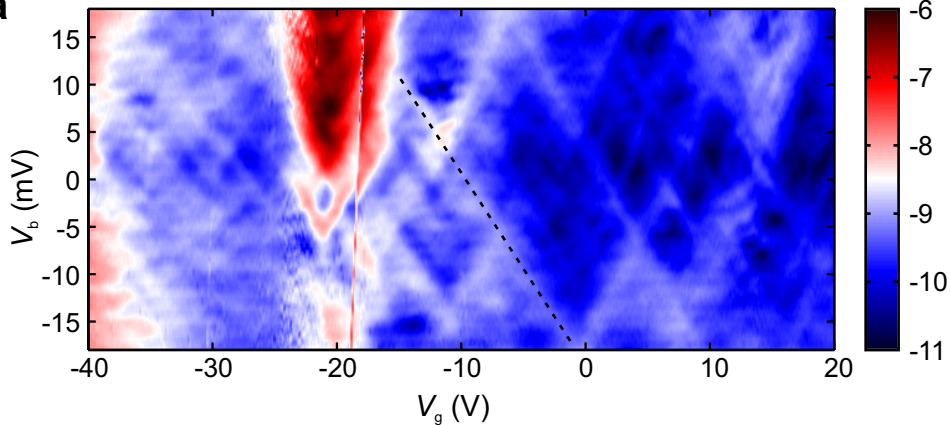
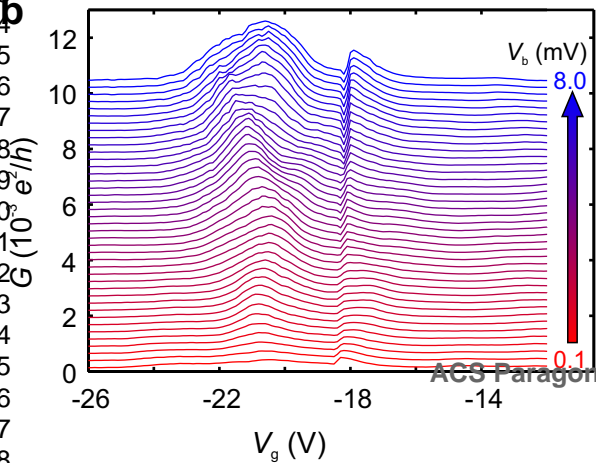
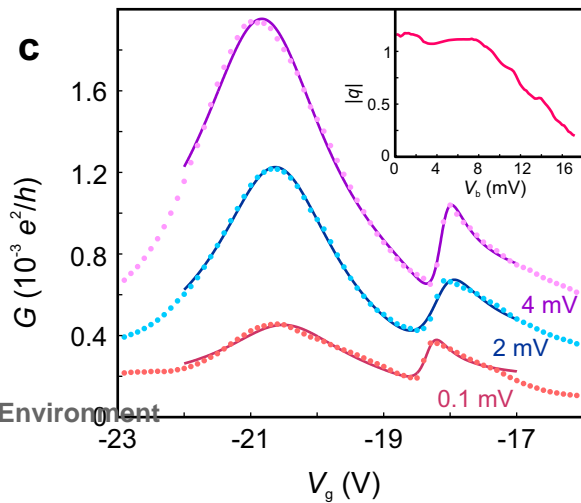
**Figure 4.** (a) Tight-binding model of a pendant state interacting with an extended 'backbone' state. The backbone is described by a chain of 5 sites with on-site energies  $\varepsilon_{1-5}$  that are coupled by hopping matrix elements  $-\gamma_{1-4}$  and coupled to the leads via the outer most sites by hopping matrix elements  $-\alpha_L$  (on the left side) and  $-\beta_R$  (on the right side). The pendant group with an on-site energy  $\varepsilon_s$  is coupled to the second site of the backbone by a hopping matrix element  $-\alpha$ . (b) Calculated transmission coefficient as a function of energy. (c), (d) Sketch of the potential profile where (c) the bias drops over the left and right contacts and (d) the bias voltage drops along the device channel. (e), (f) Corresponding conductance maps as a function of bias and gate voltage for the cases depicted in (c), (d), respectively.

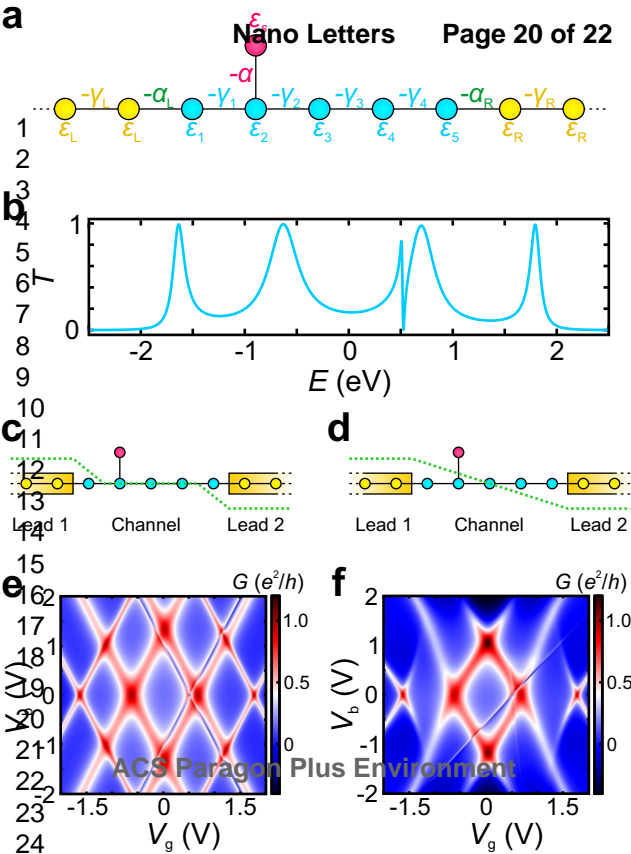


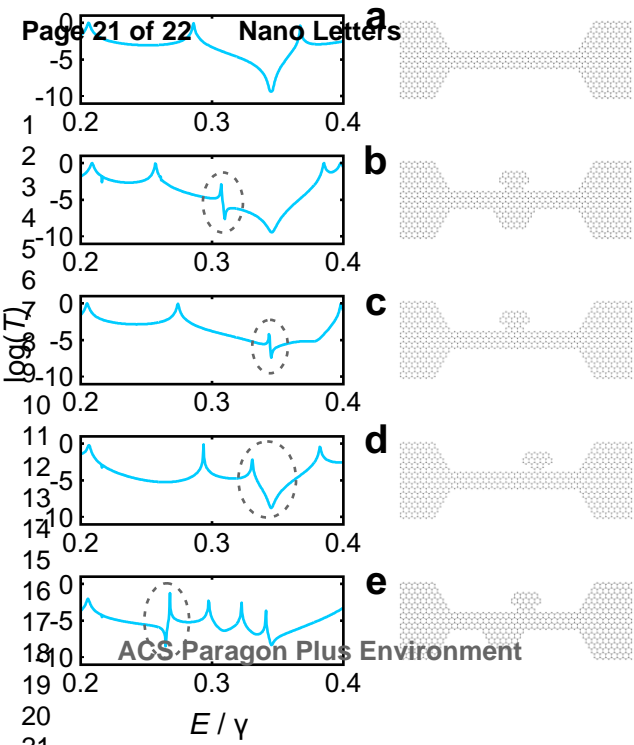
1  
2  
3 **Figure 5.** Transmission through graphene junctions. (a) Clean graphene ribbon connected to two  
4 graphene electrodes, (b-e) graphene junctions with different shape and position of pendent groups.  
5  
6  
7 The dotted circles indicate the position of Fano features.  
8  
9  
10  
11  
12  
13  
14  
15  
16  
17  
18  
19  
20  
21  
22  
23  
24  
25  
26  
27  
28  
29  
30  
31  
32  
33  
34  
35  
36  
37  
38  
39  
40  
41  
42  
43  
44  
45  
46  
47  
48  
49  
50  
51  
52  
53  
54  
55  
56  
57  
58  
59  
60

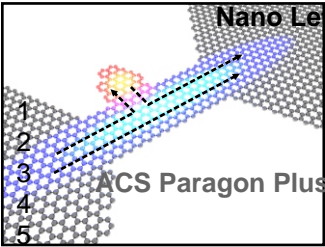




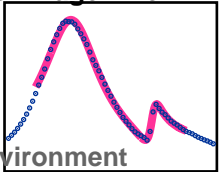
**a****b****c**







Conductance



Gate voltage

1  
2  
3  
4  
5

6